## ARTICLE     OPEN

# Origin of nanoscale heterogeneity in the surface oxide film protecting stainless steel against corrosion

Li Ma[1], Frédéric Wiame [1], Vincent Maurice [1] and Philippe Marcus[1]

Stainless steels are widely used as metal components owing to self-protection in aggressive environments, provided by an extremely thin surface oxide film enriched in chromium oxide. Yet, despite decades of research, the mechanisms distributing the chromium enrichment at small length scale are poorly understood, although it may cause loss of stability and local failure of the corrosion resistance. Here, we apply high resolution surface analysis to investigate at small time and length scales the nucleation and growth mechanisms of the surface oxide on a model stainless steel. Starting from an oxide-free surface, we report the direct observation of the oxide nucleation and local oxidation of chromium, which governs the nanoscale heterogeneity of the growing surface oxide by chromium pumping from the atomic terraces to the steps for preferential Cr(III) oxide nucleation and subsequently by segregation from the atomic planes below to grow the Cr(III) layer incompletely saturating the stainless steel surface. This work provides new insight on corrosion chemistry, by evidencing local chemical and structural defects self-generated at the nanoscale by the building process of the protective oxide barrier, and affecting the passive film stability.

## INTRODUCTION

Stainless steels (SSs) are widely used in various industrial sectors because of their high resistance to corrosion. This corrosion resistance comes from the passive film which is a surface oxide film only a few nanometers thick and strongly enriched in Cr(III) (hydr)oxide species.[1–7] Even though numerous studies have characterized the passivity of various SS grades at macroscopic level, only recent surface analytical works performed on austenitic SS have suggested that the origin of passivity breakdown, which can lead to the local failure of the corrosion resistance and to localized corrosion by pitting, would depend on the surface heterogeneity at microscopic level.[6–8] Hence, the distribution of the chromium enrichment in the passive film at the nanometric scale appears of paramount importance for the stability and barrier properties of the passive film and its resistance to localized corrosion initiation. The formation and resulting surface distribution of Cr(III) oxide and hydroxide species take place in the very early stages of surface oxidation, meaning that the initial surface changes induced by oxidation at very short time scale could determine the subsequent corrosion resistance behavior of the passivated surface, including in service conditions, and its local failure. However, to our knowledge, there is almost no study addressing the heterogeneity of SS surfaces at small space and time scales during early oxidation stages.

Such detailed insight into the initial oxidation mechanisms can be sought after with a surface science approach combining ultra-high vacuum (UHV) systems, for a very good control of the surface from metallic to oxidized state via a high precision on gaseous oxygen exposure, and single-crystalline model surfaces, for optimized control of the surface topography and structure and the effects of crystallographic defects. The surface topography modifications and the heterogeneity of the oxidation mechanisms can be investigated by scanning tunneling microscopy (STM) at the nanometric and atomic scales. Up to now, few compositional and structural studies have been performed on single-crystalline SS surfaces.[9–15] As for STM investigations on SSs, none of them addressed the detailed mechanisms of initial oxidation starting from an oxide-free surface.

Here, we show how insightful this surface science approach of initial oxidation at small length and time scales is to understand the origin of oxide film stability at the nanoscale. STM was applied to investigate at high resolution the space distribution of topographic and structural modifications occurring during initial oxidation of a single-crystalline austenitic Fe–18Cr–13Ni(100) SS surface, selected as a model surface of the widely used AISI 304 SS. The detailed characterization of the surface composition changes analyzed by X-ray photoelectron spectroscopy (XPS) was discussed elsewhere.[9] The XPS study allowed us to follow the oxidation kinetics and record composition information after successive exposures to gaseous oxygen. Starting from an oxide-free surface, it was observed that Cr(III) oxide formation was first predominant followed, with increasing oxygen uptake, by competitive formation of Fe(III) oxide species and subsequently by predominant Fe(III) oxide formation (Fig. S1). Ni did not oxidize in amounts detectable with XPS, including in the very first stages of oxide growth (Fig. S2). Combining these XPS data with the new STM data, the local nature of the oxidized model surface can be identified at various stages of the nucleation and growth of the oxide film, thus elucidating at the nanometric and atomic scale the mechanisms of the transition from the metallic to oxidized surface state at the origin of the heterogeneity in the surface oxide film forming the protection barrier against corrosion.

[1]PSL Research University, CNRS—Chimie ParisTech, Institut de Recherche de Chimie Paris (IRCP), Physical Chemistry of Surfaces Group, 11 rue Pierre et Marie Curie, 75005 Paris, France
Correspondence: Frédéric Wiame (frederic.wiame@chimie-paristech.fr) or Vincent Maurice (vincent.maurice@chimie-paristech.fr) or Philippe Marcus (philippe.marcus@chimie-paristech.fr)

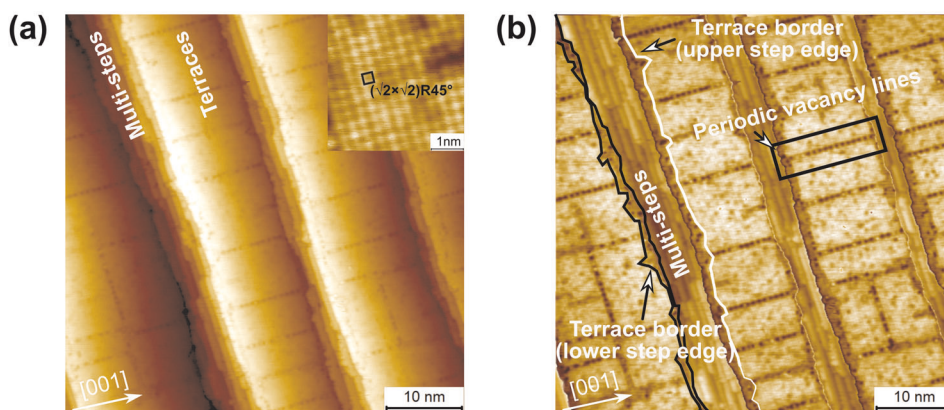**Fig. 1** Initial oxide-free stainless steel surface of Fe–18Cr–13Ni(100). **a** 50 nm × 50 nm STM image of the terrace-step topography, $I = 4.0$ nA, $V = -0.5$ V. The inset shows the atomic structure of the topmost plane on the terraces with the unit cell marked. **b** Image (**a**) obtained by leveling of the terraces and highlighting self-organization with periodic vacancy lines (one is marked). The terrace borders at the upper and lower edges of the multisteps are highlighted with white and black lines, respectively, along one of the multisteps

## RESULTS AND DISCUSSION

Figure 1 shows the topography of the initial oxide-free surface as routinely obtained prior to exposure to oxygen gas. It consists of terraces (10–20 nm wide) separated by atomic multisteps (3–6 atomic steps). The topmost plane terminating the (100)-oriented terraces contains Fe, Cr, and Ni atoms and is characterized by a $(\sqrt{2} \times \sqrt{2})R45°$ reconstructed structure with an atomic density half that of the bulk (100) planes. This atomic structure can be seen in Fig. 1a. This terrace structure is self-organized in the topmost layer with parallel and periodic lines of atom vacancies mostly aligned along the [001] direction, as better seen after terrace leveling (Fig. 1b). Self-ordering, is assigned to the minimization of the surface energy with the elastic energy associated with surface stress partly balanced by the creation energy of periodic surface defects,[16,17] vacancy lines in the present case. In the regions adjacent to both the upper and lower edges of the multisteps, the terraces appear darker. These regions of the terraces are hereafter referred to as the "terrace borders". Their darker appearance is assigned to the local presence of nitrogen, observed by XPS to co-segregate with chromium during surface preparation.[9] This structure of the as-prepared surface will be discussed in further details in a separate paper.

Nucleation of the surface oxide
Figure 2 shows the very first stage of oxide nucleation as observed after an exposure to oxygen of 0.96 L. At atmospheric pressure, a 1 L exposure corresponds to an exposure time of about 1 ns, meaning that we reveal here the oxide nucleation mechanisms thought to occur at extremely short time scale at ambient pressure. The initial topography of alternating atomic multisteps and terraces is still observed. On the terraces, the reconstructed lattice of the topmost plane and the periodic vacancy lines of the initial surface remain present. However, three main local surface alterations are observed.

At the multisteps, the surface is saturated, at least locally, by newly formed square-shaped islands, as highlighted by the marked rectangle in Fig. 2a and enlarged in Fig. 2e. Since Cr(III) oxide species are preferentially formed in the very first stages of oxidation up to 10 L (Fig. S1),[9] these square-shaped islands are assigned to the Cr(III) oxide nuclei. Incorporation of $Fe^{2+/3+}$ cations in these nuclei cannot be excluded. The apparent height difference between the nuclei situated at two consecutive atomic layers is about 0.18–0.20 nm, in agreement with the reticular distance between successive (100) planes of the alloy (0.18 nm), meaning that the edge of each atomic layer of the alloy has reacted with formation of chromium-rich oxide nuclei. This local

preferential nucleation is a direct consequence of the lower coordination and thus higher reactivity of the atoms at the edges of the atomic layers. Chromium, co-segregated with nitrogen on the initial surface and enriched at the terrace borders, also plays a role in the local preferential nucleation because of its vicinity with the step edges. The size of these oxide nuclei is about 1.5–2.0 nm. Corrugations inside the oxide nuclei are also revealed with interdistances of about 0.4–0.5 nm along the ⟨011⟩ directions (Fig. 2e), however, with no formation of extended periodic patterns due to the small size. Their square shape is thought to result from morphological constraints imposed by the symmetry of the substrate structure, as commonly observed with nanostructures.[17]

On the terraces, no superstructure of dissociatively chemisorbed oxygen was observed, such as formed on Ni(100) for example,[18] suggesting surface diffusion of adsorbed oxygen at 250 °C and capture by the formation of the oxide nuclei during the elapsed time (about 10 min at $2 \times 10^{-9}$ mbar) of the 1 L oxygen exposure. New vacancy patterns were formed between the vacancy lines initially present (Fig. 2b). One of them is shown at atomic resolution in Fig. 2c. The line profile in Fig. 2d shows that it consists of vacancy lines appearing about 40 pm lower than the reconstructed terrace, like for the periodic vacancy lines on the clean surface, and their width is about 0.8–0.9 nm, i.e., slightly narrower than that (1.05 nm) of the periodic vacancy lines. These new vacancy lines are thus assigned to rows of single atom vacancies formed in the topmost reconstructed plane and aligned along the ⟨001⟩ and ⟨011⟩ directions. One can notice that the patterns formed by these new vacancy rows are for most of them connected to the initial periodic vacancy lines and/or to the modified terrace borders adjacent to the upper edges of the multisteps, indicating the formation of diffusion pathways leading to the multisteps and thus to the Cr(III)-rich oxide nuclei. The atomic corrugations inside these vacancy patterns appear lower (Fig. 2d), and their arrangement slightly distorted compared to the normal reconstructed lattice.

At the terrace borders adjacent to the upper edge of the multisteps, new vacancy patterns are also formed (Fig. 2b). These new vacancy patterns consist of vacancy lines for most of them aligned along the ⟨011⟩ directions. The apparent height difference relative to the reconstructed terrace is about 40 pm, the same as for the vacancy rows on the terraces. Moreover, the atomic arrangements in the vacancy patterns at the terrace borders and on the terraces appear similarly lower compared to the normal reconstructed lattice (Fig. 2c). Thus, the vacancy patterns formed at the terrace borders can be considered as having the same origin as those formed on the terraces and correspond to the modified surface locally resulting from the preferential
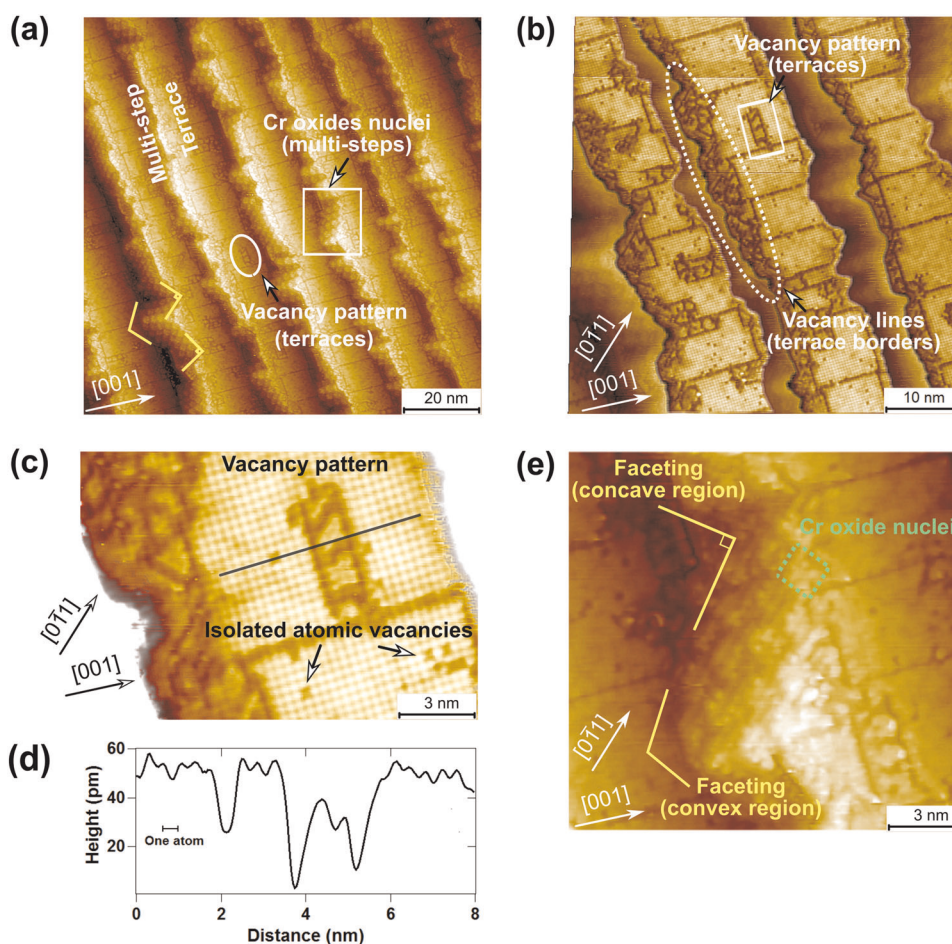
**Fig. 2** Initial oxide nucleation after an oxygen exposure of 0.96 L at 250 °C. **a** 100 nm × 100 nm STM image of terraces modified by new vacancy patterns and multisteps saturated with oxide nuclei, $I = 0.2$ nA, $V = 0.7$ V. **b** 50 nm × 50 nm STM image highlighting the new vacancy patterns formed on the terraces, $I = 0.2$ nA, $V = -0.7$ V, terrace leveling. **c** Atomic structure of the vacancy pattern marked in (**b**), $I = 0.2$ nA, $V = -0.7$ V. **d** Profile of the line marked in (**c**). **e** Enlarged image of the multistep marked by a rectangle in (**a**) and saturated by oxide nuclei, $I = 0.2$ nA, $V = 0.7$ V. One of the oxide nuclei is marked by a dotted square

consumption of chromium by the oxidation reaction. This view is further supported by the isolated atomic depressions which are also observed at the atomic positions (nods) of the reconstructed lattice of the terraces (Fig. 2c) and have the unambiguous size of a vacancy with a depth similar to that of the periodic vacancy lines. They can also be identified as vacancies left by the diffusion of chromium atoms to the nucleation sites of the oxide located at the atomic multisteps.

As marked in Fig. 2a, e, the oxidized multisteps present concave and convex regions resulting from the alignment of the oxide nuclei formed at each step edge along two main orientations: one rotated by 45° ± 2°, 50° ± 3°, or 56° ± 3° from the [001] direction (i.e., toward [0–11]) and the other rotated by −28° ± 2° with respect to [001] (i.e., toward [011]). Since unseen prior to oxidation (Fig. 1), these local re-orientations of the steps suggest that faceting has been induced by the nucleation mechanism. The earliest oxide nuclei could be formed at the concave regions and their formation propagate along the edges of each atomic plane and stop at the convex regions where the propagation directions would meet at local saturation of the multisteps. The Cr atoms feeding the formation of the oxide nuclei would be consumed at the edge of each atomic layer of the multisteps but also on the terraces, preferentially at their borders because of their closer vicinity from the multistep edges.

Figure 3 shows the secondary stage of oxide nucleation as observed after an oxygen exposure of 2.97 L. The number of oxide nuclei formed at the multistep edges has increased thereby decreasing the width of the narrowest terraces to less than 10 nm. New square-shaped islands, also assigned to chromium oxide nuclei on the basis of XPS analysis,[9] formed on the terraces as well. These new square-shaped oxide nuclei have their sides aligned along the ⟨011⟩ directions, like those at the steps. They form a defective square lattice also oriented along the ⟨011⟩ directions and with a parameter of 2.8 ± 0.2 nm, indicative of local self-organization of the oxide nuclei. Their coverage ratio on the terraces is about 20%. The apparent height of these oxide nuclei is about 0.26 ± 0.02 nm compared to the unoxidized terraces, which is larger than the reticular distance of the (100)-oriented alloy (0.18 nm). Their average size is 2.1 ± 0.1 nm, similar to that of the oxide nuclei formed at the multisteps and about 6 times the reconstructed lattice parameter (0.359 nm). The corrugations inside these new oxide nuclei are aligned along the ⟨011⟩ directions, like for the oxide nuclei at the multisteps, at a distance of 0.5 nm (Fig. 3d).

The terraces not yet oxidized but modified by Cr depletion due to nearby formation of oxide nuclei do not show the reconstructed structure anymore, as seen for example in the region marked as "lifted reconstruction" in Fig. 3a. The initial periodic vacancy lines and the vacancy pattern observed at 1 L exposure are no longer present. Fast Fourier transform of these local areas confirms no ordered structure and the atomic arrangement appears thus disordered as a result of further injection of
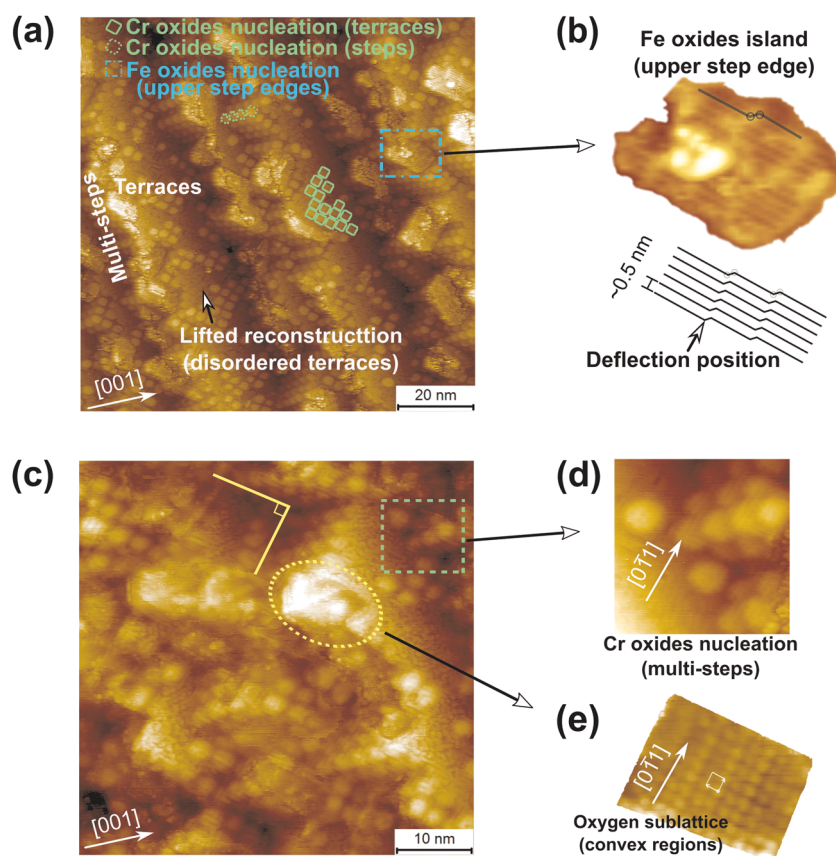
**Fig. 3** Delayed oxide nucleation after an oxygen exposure of 2.91 L at 250 °C. **a** 100 nm × 100 nm STM image of terraces and multisteps modified by oxide nucleation as marked, $I = 0.2$ nA, $V = −2.0$ V. **b** Enlarged image and modeling of Fe oxide island with linear pattern near upper step edge in (**a**). **c** 50 nm × 50 nm STM image of modified terraces and multisteps, $I = 0.2$ nA, $V = −0.7$ V. **d** Enlarged image of square-shaped oxide nuclei at multisteps in (**c**), $I = 0.2$ nA, $V = −0.7$ V. **e** Image of oxygen sub-lattice at convex oxidized step region in (**c**), $I = 2.0$ nA, $V = −0.4$ V

vacancies to feed the continuous formation of the new chromium oxide nuclei.

At the upper edges of the multisteps, a different structure appearing brighter than the disordered terraces is developed locally. One example is marked by the dotted blue rectangle in Fig. 3a and enlarged in Fig. 3b. Contrary to square oxide nuclei, this structure forms only at the topmost atomic layer near the multistep edges, not at every edges of the multisteps. It is also observed preferentially at the convex regions of the multisteps, assigned above to the latest site of oxide nucleation at the multisteps. It displays a line pattern observed in at least four orientations: $45° ± 2°$, $80° ± 2°$, $110° ± 2°$, and $135° ± 3°$, with respect to the [001] direction. The average apparent height is $0.17 ± 0.02$ nm relative to the disordered terrace, i.e., lower than for the square-shaped Cr(III) oxide nuclei. An atomic image and schematic layout is presented in Fig. 3b. It consists in parallel lines with a periodicity of 0.4–0.5 nm, deflected every 2.5–4.0 nm in length of a half period (0.20–0.25 nm) and with deflection position depending on the size of the line pattern. According to XPS,[9] a small quantity of $Fe^{2+}$ is formed at 3 L and the quantity of $Fe^{3+}$ is lower than that of $Fe^{2+}$. Therefore, this local structure could correspond to the nucleation of a Fe(II)-containing oxide. More-over, it is quite similar to the morphology of the $(2\sqrt{2} × \sqrt{2})$R45°-reconstructed $Fe_3O_4(001)$ surface prepared by annealing under UHV at 250–500 °C,[19] which lattice parameter is 0.6 nm. It shows as well bright spots located between the atomic rows separated by about 0.5 nm in the $\langle011\rangle$ directions, assigned to tetrahedral sites of the octahedral lattice. Since $Fe_3O_4(001)$ is very sensitive to surface preparation method, the $(2\sqrt{2} × \sqrt{2})$R45° reconstruction

can be converted to $(\sqrt{2} × \sqrt{2})$R45° of $Fe_3O_4(001)$ by heating in oxygen,[19] the latter being the typical morphology of the $Fe_3O_4(001)$ observed by STM.[20,21] Thus the line structure shown in Fig. 3b is suggested to be a 2D iron oxide island adopting a structure close to that of the reduced $Fe_3O_4(001)$ surface.

Figure 3e shows the atomic resolution image of an apex of the convex region of the multisteps marked in Fig. 3c. This structure is about 60 pm lower than the disordered terrace, thus lower than the square-shaped oxide nuclei and the line patterns. The square atomic lattice is oriented at $46° ± 2°$ compared to [001] and the average lattice parameter is $0.285 ± 0.005$ nm. This atomic lattice is consistent with the O sublattices in iron oxides which have lattice parameters of 0.29–0.30 nm[22] and thus could correspond to the precursor O sublattice of the oxide crystallites that subsequently develop at the convex regions of the oxidized multisteps after further exposure to oxygen and that contain iron cations according to XPS analysis.

Nanoscale surface heterogeneity is thus generated already in the oxide nucleation phase by the mechanism of preferential local supply of metallic Cr feeding the formation of Cr(III)-rich oxide nuclei (Fig. 4). Cr(III) oxide nucleation is instantaneous at 1 L exposure and preferentially takes place at the sites of reduced atomic coordination of the metallic alloy, thus nearly saturating the multisteps. It consumes Cr atoms locally present at each atomic edge of the multisteps but also remote Cr atoms diffusing to the nucleation sites and leaving behind Cr vacancies in the topmost layer of the terraces (Fig. 4a, b). The locally Cr-depleted regions of the topmost atomic layer rearrange with formation of vacancy patterns. The terrace borders adjacent to the upper edge
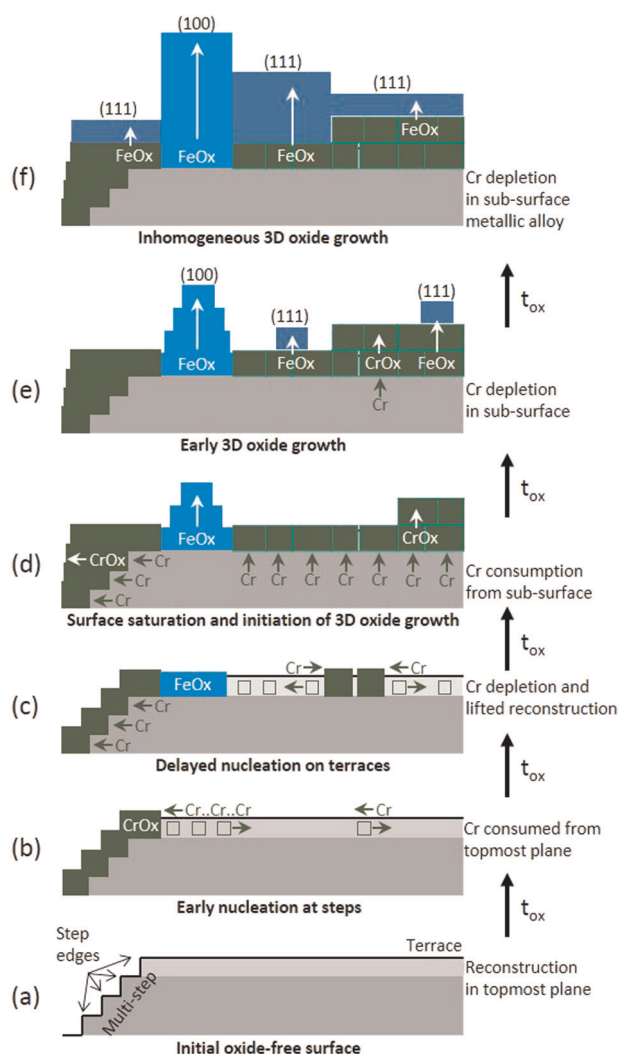
**Fig. 4** Cross-section model of early oxidation mechanisms at the origin of the nanoscale heterogeinity of the surface oxide film on austenitic stainless steel (heigth-to-width aspect ratio is not to scale). **a** Initial oxide-free surface with atomic multisteps and terraces. **b** Early Cr oxide nucleation at the multisteps and Cr consumption with vacancy injection in topmost layer of terraces. **c** Delayed Cr and Fe oxides nucleation on terraces fully depleting Cr in the topmost plane. **d** Mixed oxide layer at surface saturation formed by Cr and Fe transport from the metallic planes below the oxide. **e** Early inhomogeneous 3D growth of iron oxide through interfacial Cr oxide barrier layer or directly on SS substrate. **f** Inhomogeneous 3D growth of iron oxides after Cr depletion of metallic alloy below the oxide film

of the multisteps are preferentially rearranged compared to the terrace centers as an effect of their closer vicinity from the initial oxide nucleation sites and their initial Cr enrichment by segregation. The vacancy lines of the initial terrace structure remain stable as well as the reconstructed superstructure. The initial built up of the oxide nuclei at step edges is preferential along the $\langle 011 \rangle$ substrate directions leading to the formation of square-shaped Cr(III)-rich oxide nuclei. Propagation of the nucleation along the step edges occurs in two preferential orientations leading to the faceting of the multisteps with formation of concave and convex apexes at saturation.

Delayed Cr(III) oxide nucleation takes place on the terraces away from the step edges and most likely in sites not yet or less depleted in Cr (Fig. 4c). It is also fed by Cr preferential vacancy injection in the nearby areas leading to further Cr depletion of the

not yet oxidized terraces in agreement with the preferential consumption of metallic chromium observed by XPS[9] (Fig. S1). The reconstruction characterizing the initial surface is fully lifted with loss of structural order. In the local regions where all chromium initially present is oxidized and the most remote from the remaining sources of Cr supply, i.e., at the terrace borders adjacent to the convex apexes of the multisteps, the oxidation of iron takes place, leading to the local formation of Fe-containing (predominantly Fe(II)) oxide islands of morphology and structure different from those of the Cr(III)-rich square-shaped oxide nuclei.

Oxide layer at saturation of the surface coverage
Figure 5 shows the surface morphology at saturation of the surface coverage by the oxide layer as obtained after an oxygen exposure of 9.24 L. The initial succession of terraces is still observed but there are no longer square-shaped oxide nuclei nor unoxidized disordered terraces. The surface is now fully covered by an oxide layer, Cr(III)-rich according to XPS[9] and consisting of patches, relatively close-packed and observed both on terraces and at terrace borders. In some local areas, the oxide patches locally form a distorted hexagonal pattern, detailed in Fig. 5c, with one close-packed direction oriented nearly parallel to $[0\bar{1}1]$. The size of the oxide patches is about $1.6 \pm 0.2$ nm. The hexagonal shape of some patches suggests the growth of a Cr(III)-rich oxide grains adopting, at least locally, the $\alpha$-Cr(III)$_2$O$_3$ corundum structure[23] with the (0001) basal plane oriented parallel to the (100) plane of the SS substrate. The transition from a surface covered by square-shaped Cr(III)-rich oxide nuclei and Cr-depleted unoxidized areas at 3 L to a surface fully covered by a layer of Cr(III)-rich oxide grains at 10 L must involve the additional supply of chromium from the substrate planes below the topmost atomic plane, thus suggesting that a 3D mechanism of atomic transport has been triggered and that the oxide grains result from the segregation of additional Cr to the topmost surface. Preferential consumption of metallic Cr from the alloy was confirmed by XPS[9] (Fig. S1). The evolution from square-shaped Cr(III)-rich nuclei of small size at 1–3 L to a granular Cr(III)-rich layer with local hexagonal symmetry may result from modified local crystallization and a reduced effect of the constraints imposed by the substrate structure.

At this point the 3D growth of the surface oxide has been initiated. At the multisteps, this is supported by the fact that the square-shaped oxide nuclei are no longer observed, and thus 3D Cr(III)-rich oxide grains saturate the multisteps likely after coalescence of the oxide nuclei formed at each atomic step edge. On the terraces, this is proven by the formation of new layers of close-packed granular oxide. One example is labeled E on terrace B (Fig. 5b) with a apparent height of about 0.25 nm, higher than the alloy reticular distance (0.18 nm) and thus consistent with the triggered formation of a multilayered Cr(III)-rich oxide layer.

The growth of 3D oxide islands thicker than the Cr(III)-rich oxide layer covering the terraces is also observed, predominantly near the multistep upper edges where Cr is likely fully depleted in the substrate owing to the saturation of the multisteps by 3D Cr(III)-rich oxide grains. As observed in Fig. 5b, these 3D oxide islands appear in the form of amorphous clusters of oxide patches. Line profile analysis (Fig. 5d) shows that the oxide islands apparent height varies from 0.2 to 0.8 nm compared to their respective terraces, confirming the triggered 3D growth of oxide patches. This locally thicker 3D oxide islands indicates the formation of faster growing oxide species likely enriched in Fe(III) and Fe(II) according to XPS,[9] thus showing that the oxide layer has heterogeneous nanoscale morphology and composition also at saturation of the surface coverage prior to further 3D growth. This is schematically represented in Fig. 4d.
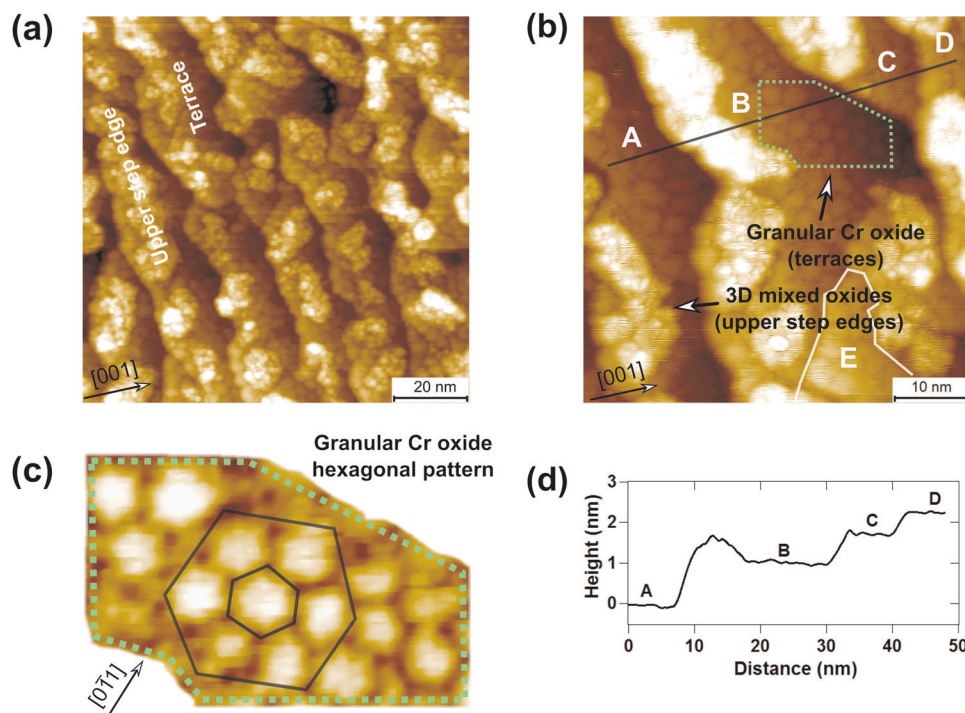
**Fig. 5** Oxide layer at saturation of the surface coverage after an oxygen exposure of 9.24 L at 250 °C. **a** 100 nm × 100 nm STM image of modified terraces and multisteps, $I = 0.5$ nA, $V = 1.0$ V. **b** 50 nm × 50 nm STM image of granular oxide covering the terraces and 3D oxide islands near upper step edges, $I = 1.0$ nA, $V = 2.0$ V. **c** Enlarged image of granular oxide layer as marked in (**b**), $I = 1.0$ nA, $V = 2.0$ V. **d** Profile of the marked line in (**b**). A–D refer to the different substrate terraces observed along the marked line in (**b**). E refers to a new topographic level on terrace B

### Three-dimensional growth of the surface oxide layer

With increasing oxygen uptake of the surface, the Cr(III)-rich nanogranular oxide layer gradually develops a more compact and better ordered hexagonal structure thanks to further Cr segregation from the substrate. Concomitantly, the iron-rich islands increase in apparent height (i.e., thickness) and develop morphologies consistent with the formation of (100)-oriented iron oxide structures. This is illustrated in Fig. 6 by the surface morphology observed after a 97.5 L oxygen exposure (an intermediate morphology is shown in Fig. S3). The terraces are increasingly covered by 3D oxide islands of increased apparent height. The granular oxide layer saturating the terraces is still observed between the 3D oxide islands. The hexagonal pattern of oxide grains highlighted in Fig. 6b is consistent with the Cr(III)$_2$O$_3$ corundum structure[23] with the (0001) basal plane oriented parallel to the (100) plane of the SS substrate. The increased apparent height of the 3D islands is evidenced by the profile shown Fig. 6b. The brightest island I4 is about 1.7 nm higher than terrace T3. Other 3D islands along this profile show an apparent height difference of 0.5–1.0 nm compared to their respective terraces. The highest island in Fig. 6a has an apparent height of 2.5–3.0 nm.

The formation of crystalline structures is also evidenced by the shape of the 3D islands. Some, including the highest, develop a rectangular morphology (marked by dotted rectangles in Fig. 6a, b) while others develop a triangular morphology (marked by the dotted triangle in Fig. 6a). For both type of morphologies, at least one side of the islands is oriented along one of the ⟨011⟩ directions of the substrate, indicating epitaxial relationships between the oxide island structures and the substrate. The triangular oxide islands likely consist of iron oxide as supported by XPS[9] and could correspond to (111)-oriented crystallites adopting structures of trigonal symmetry like those of FeO,[24] Fe$_3$O$_4$,[22,25] or γ-Fe$_2$O$_3$.[22] Since (0001)-oriented α-Fe$_2$O$_3$ presents a hexagonal structure based on STM examinations,[22,26] this possibility is not

retained at this stage. γ-Fe$_2$O$_3$ is isostructural to Fe$_3$O$_4$ and the two structures can hardly be differentiated.[22]

A 3D image of adjacent rectangular islands is shown in Fig. 6c, confirming the multilayered growth of crystalline oxide islands. The regions A–C present a step structure with a step apparent height of about 0.5 nm (Fig. 6d). Some protrusions are observed at the top of the rectangular islands which made the atomic arrangement of the top layer difficult to image. A line pattern with similar characteristics as shown in Fig. 3b was observed. Since, at this stage, continuing oxide growth is characterized by iron oxides formation, essentially Fe(III) species, and almost no chromium oxide formation according to XPS,[9] these growing rectangular islands are assigned to iron oxides and could correspond to (100)-oriented crystallites adopting a structure common to Fe$_3$O$_4$ and γ-Fe$_2$O$_3$. According to literature,[27] Fe$_3$O$_4$ thin films formed on MgO (001) cannot be oxidized to γ-Fe$_2$O$_3$. The protrusions observed at the top of the islands are consistent with a 3D growth proceeding by cation transport to the oxide/gas interface and point to sites of nucleation on the oxide surface.

Figure 7 shows the surface morphology after further 3D growth of the surface oxide film (oxygen exposure of 191.4 L). The original terrace and multistep structure has for the most part disappeared, but the hexagonal close-packed pattern of oxide grains formerly covering the terraces can still be observed in local areas (as seen in the inset Fig. 7a). This locally subsisting structure is assigned to the Cr(III)-rich oxide initially formed at the interface with the alloy and adopting the (0001)-oriented α-Cr$_2$O$_3$ structure. The continuing 3D growth of rectangular islands (Fig. 7a, b) is now concomitant with the development of extended flat regions of hexagonal morphology (Fig. 7a, c, d). The rectangular islands have now an apparent height of more than 3 nm compared to neighboring flat regions, evidencing their continuous faster 3D growth. Their sides are still oriented along the ⟨011⟩ substrate directions, with a length varying from 10 to 20 nm. The top layer is not flat with a tilt angle of 2°–4° in the [0$\bar{1}$1] substrate direction
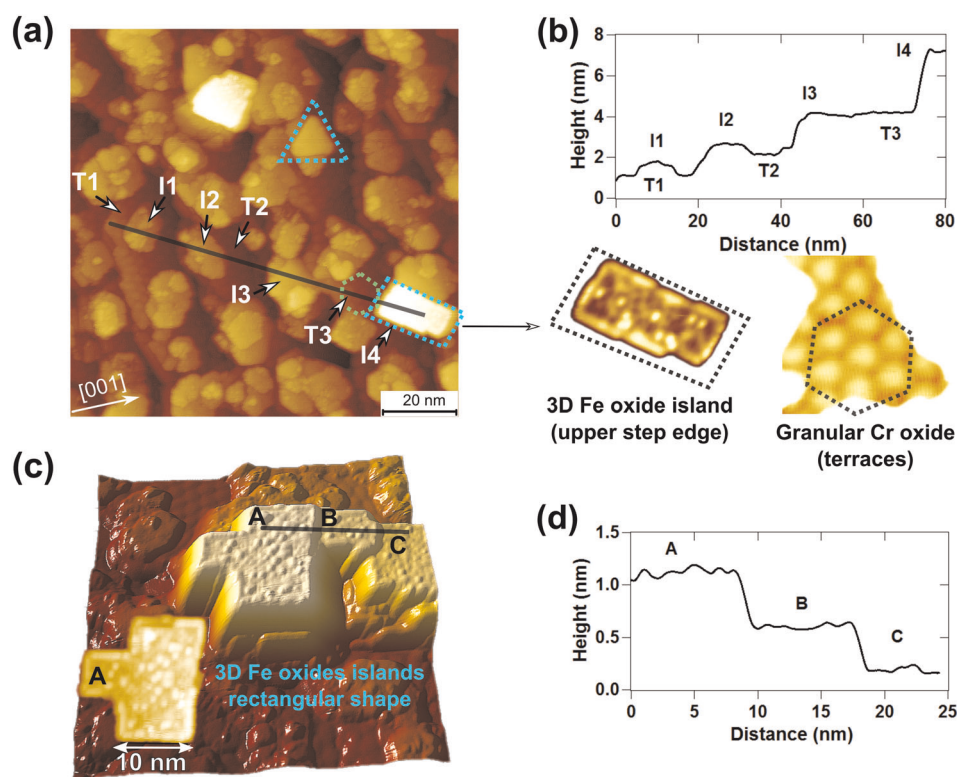
**Fig. 6** Oxide layer with heterogeneous 3D island growth after an oxygen exposure of 97.5 L at 250 °C. **a** 100 nm × 100 nm STM image of modified terraces and multisteps, $I = 0.5$ nA, $V = 2.5$ V. **b** Profile of the marked line in (**a**) and enlarged rectangular island and hexagonal pattern marked in (**a**). **c** 3D view of rectangular islands, 50 nm × 50 nm, $I = 0.5$ nA, $V = 2.5$ V. Top view of island A is superimposed. **d** Profile of the marked line in (**c**). T refers to terraces and I refers to islands

compared with the (001) substrate plane, possibly as a result of their layer-by-layer growth at the outermost surface. Like after the 97.5 L exposure, these continuously growing 3D crystalline oxide islands are assigned to (100)-oriented crystallites adopting a $Fe_3O_4$-like structure. Their layer-by-layer growth at the outermost surface is consistent with a growth mechanism involving the transport of cation through the oxide.

The development of extended flat regions of hexagonal morphology is indicative of the further 3D growth of the triangular oxide islands observed after shorter exposures. In Fig. 7c, d, it can be seen that one edge of these hexagonal terraces is oriented parallel to the $[0\bar{1}1]$ direction, thereby indicating a similar orientation and thus epitaxy as for the triangular oxide islands observed after shorter exposures. The step apparent height between successive hexagonal terraces is 0.25–0.30 nm. This value is in agreement with the reticular distance between successive planes of the O sub-lattice in iron oxides (0.304 nm in FeO(111), 0.248 nm in $Fe_3O_4$(111), 0.229 nm in $\alpha$-$Fe_2O_3$ (0001)[22]), showing, whatever the oxide grown, a plane-by-plane 3D growth mechanism also involving cation transport through the oxide lattice.

Figure 7e shows the atomic structure measured on the terraces and including the dark spots marked in Fig. 7c, d. It consists of hexagons alternating two types of structures in triangular domains marked by dotted and solid lines. The dark spots correspond to the nodes joining six domains. This hexagonal pattern is similar to that observed by STM for epitaxial $Fe_3O_4$(111) films grown on Pt (111) by iron deposition and then oxidation in oxygen gas[28] and for $Fe_3O_4$ mineral specimen,[29] and interpreted as a two-phase superstructure alternating $Fe_3O_4$(111) and FeO(111) domains. Here, the dotted triangles show a hexagonal lattice with a unit cell parameter of $0.60 \pm 0.05$ nm fitting a ($2 \times 2$) superstructure with respect to the hexagonal closed-packed planes of the O sub-lattice in iron oxides. It is consistent with the close-packed layers

of tetrahedrally coordinated Fe atoms in the $Fe_3O_4$(111) structure, which bulk lattice parameter is $0.590 \pm 0.004$ nm.[30] The solid triangle region shows a hexagonal lattice rotated by 30° and with a unit cell parameter of $0.52 \pm 0.03$ nm. This parameter fits a ($\sqrt{3} \times \sqrt{3}$)R30° superstructure with respect of the hexagonal closed-packed planes of the O sub-lattice in iron oxides. It could be associated with the Fe sublattice in the $\alpha$-$Fe_2O_3$(0001), whose bulk lattice parameter is 0.5 nm.[26,31,32] Schematic atomic modeling is shown in Fig. 7f. Figure 7e also shows that the two types of domains are at the same topographic level, but with some atomic protrusions in the dotted triangles appearing 30–40 pm higher. These protrusions could be the oxygen atoms on the terminating iron atoms.

These data show that when 3D oxide growth becomes the dominant oxidation mechanism, the Cr(III)-rich nanogranular oxide layer gradually develops a more compact and better ordered hexagonal structure, causing Cr depletion in the underlying modified metallic phase. At this stage, triangular-shaped islands nucleate as a result of the transport of iron to the topmost surface and further develop to predominantly cover the surface with morphologies consistent with (111)-oriented or (0001)-oriented iron oxide structures. Concomitantly the iron-rich islands initially directly nucleated on the alloy surface faster increase in thickness, also by cation transport to the outermost surface, and develop protruding island morphologies consistent with (100)-oriented iron oxide structures (Fig. 4e, f).

This study provides direct evidence that the surface oxide film on SS contains nanoscale heterogeneities of composition and structure, even when grown on a substrate of well-controlled crystallographic orientation and free of microcrystalline defects. The nanoscale heterogeneity of the surface oxide originates from the mechanism of chromium pumping from atomic terraces to the multisteps for formation of Cr(III)-rich oxide nuclei. Subsequently,
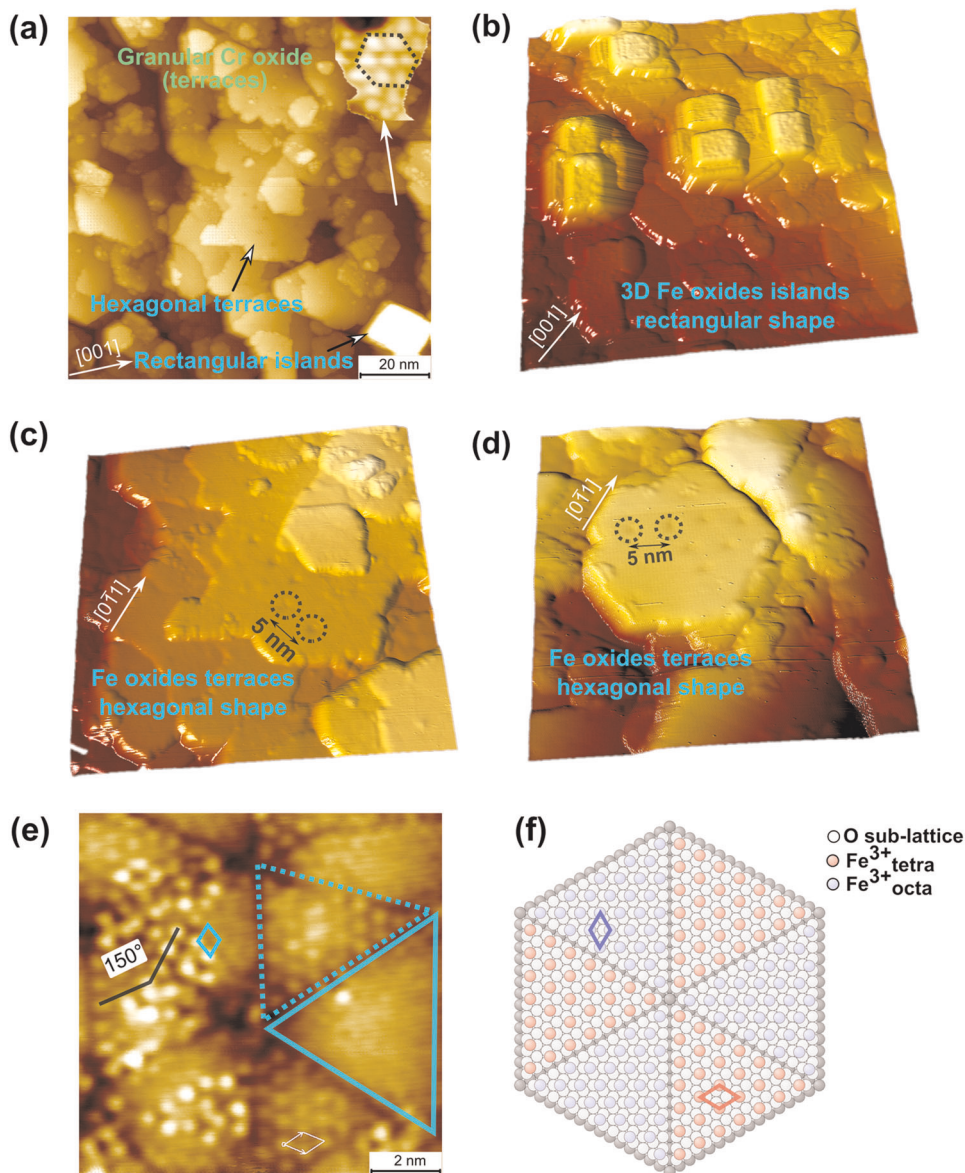
**Fig. 7** Inhomogeneous 3D multilayered oxide film after an oxygen exposure of 191.4 L at 250 °C. **a** 100 nm × 100 nm STM image of surface oxide topography, $I = 0.2$ nA, $V = 2.0$ V. The inset marked by a hexagon is an enlarged view of the granular Cr oxide interfacial layer observed locally. **b** 3D view image of rectangular-shaped islands, 50 nm × 50 nm, $I = 0.5$ nA, $V = 2.0$ V. **c** 3D view of flat terraces area, 50 nm × 50 nm, $I = 0.5$ nA, $V = 2.5$ V. **d** 3D view of hexagonal terraces, 50 nm × 50 nm, $I = 0.5$ nA, $V = 2.5$ V. **e** Atomic structure on hexagonal terrace in (**d**), 10 nm × 10 nm, $I = 0.2$ nA, $V = -2.0$ V. Domains and unit cells are marked. **f** Atomic model of hexagonal structure in (**e**)

segregation from the atomic planes below takes place to build the Cr(III)-rich layer nearly saturating the SS surface except at terrace borders adjacent to step edges where the three-dimensional growth of iron-rich islands is initiated. After Cr depletion in the metallic layers below the surface oxide, the heterogeneity of the growing three-dimensional multilayered iron oxide is related to the barrier properties of the interfacial Cr(III)-rich oxide formed at saturation of the surface coverage.

This work allows us to better understand the factors governing the stability of protective surface oxide films, in particular the local chemical and structural defects self-generated by the oxidation process. It brings important new insight into the nature and the mechanisms of formation of surface oxides and their impact on the initiation of localized corrosion, with breakdown being expected in the least Cr(III)-enriched regions of the surface oxide and self-repair expected to be ineffective in the metallic surface regions depleted in Cr.

## METHODS

The same (100)-oriented single crystal of Fe–18Cr–13Ni (at%) composition and 99.999% purity as for the XPS study was used.[9] The composition is close to the one of 304 SS. The surface was pretreated by mechanical and electrochemical polishing before introduction under UHV, as described previously.[12]

In order to achieve in situ observations of early oxidation stages, the experiments were performed in UHV conditions where different analytical techniques are connected and can be applied without breaking the vacuum. The base pressure in the UHV platform was below $10^{-10}$ mbar. After introduction of the sample in the UHV system, the sample surface was cleaned by cycles of $Ar^+$ ion sputtering (1 kV, 10 μA, 10 min) and annealing (700 °C, 10 min) in the preparation chamber. Surface cleanness and typical structure reconstruction were examined by XPS and low energy electron diffraction, respectively. The temperature of 250 °C was chosen as oxidation temperature because it is of interest for various practical applications. The oxidation kinetics and the associated compositional surface changes were examined by XPS,[9] and similar oxidation conditions were used in this work. Oxygen exposure was calculated precisely by

integration of recorded oxygen pressure in the UHV chamber as a function of exposure time. The oxygen pressure was controlled and recorded below $10^{-8}$ mbar to follow the very low exposures to less than 200 L (1 L = 1.33 × $10^{-6}$ mbar s) with a 0.01 L uncertainty on reported exposure values. The elapsed time for each step of exposure was of 6–10 min with increasing pressure in order to achieve higher exposures.

The STM experiments were conducted with a VT STM XA from Scienta Omicron on newly prepared samples for each studied exposure. Tungsten tips chemically etched in NaOH aqueous solution were used. After introduction under UHV, they were further prepared by heating, voltage pulses and high voltage scanning. The STM images were acquired in constant current mode. The drift was corrected during scan and the scanner calibration was performed by comparison to reference lattice parameters in case of atomically resolved images. Terrace leveling was performed by correcting the slope of the terraces and suppressing their height differences. Image contrast was adjusted to gain more details in local areas of interest.

## DATA AVAILABILITY

The data that support the findings of this study are available from the corresponding author upon reasonable request.

## AUTHOR CONTRIBUTIONS

The study was conceived by V.M. and P.M. with the assistance of F.W. L.M. performed surface preparation, STM experiments and data acquisition and analysis under the supervision of F.W. All authors discussed the data interpretation. L.M. wrote the paper first draft, revised by F.W., V.M., and P.M. All authors approved the final version.

## ADDITIONAL INFORMATION

**Supplementary information** accompanies the paper on the *npj Materials Degradation* website (https://doi.org/10.1038/s41529-019-0091-4).

**Competing interests:** The authors declare no competing interests.

**Publisher's note:** Springer Nature remains neutral with regard to jurisdictional claims in published maps and institutional affiliations.

## REFERENCES

1. Macdonald, D. Passivity—the key to our metals-based civilization. *Pure Appl. Chem.* **71**, 951–978 (1999).
2. Strehblow, H.-H., Maurice, V. & Marcus, P. Passivity of metals. in (ed P. Marcus), *Corrosion Mechanisms in Theory and Practice*, third edition (Taylor and Francis, CRC Press, 2011) pp. 235–326.
3. Marcus, P. & Maurice, V. Oxide passive films and corrosion protection. in (eds G. Pacchioni & S. Valeri) *Science and Technology* (Wiley-VCH Verlag GmbH & Co. KGaA, Weinheim, 2012) pp. 119–144.
4. Olsson, C. & Landolt, D. Passive films on stainless steels—chemistry, structure and growth. *Electrochim. Acta* **48**, 1093–1104 (2003).
5. Strehblow, H.-H. Passivity of metals studied by surface analytical methods, a review. *Electrochim. Acta* **212**, 630–648 (2016).
6. Maurice, V. & Marcus, P. Current developments of nanoscale insight into corrosion protection by passive oxide films. *Curr. Opin. Solid State Mater. Sci.* **22**, 156–167 (2018).
7. Maurice, V. et al. Effects of molybdenum on the composition and nanoscale morphology of passivated austenitic stainless steel surfaces. *Faraday Discuss.* **180**, 151–170 (2015).
8. Massoud, T., Maurice, V., Klein, L. H., Seyeux, A. & Marcus, P. Nanostructure and local properties of oxide layers grown on stainless steel in simulated pressurized water reactor environment. *Corros. Sci.* **84**, 198–203 (2014).
9. Ma, L., Wiame, F., Maurice, V. & Marcus, P. New insight on early oxidation stages of austenitic stainless steel from in situ XPS analysis on single-crystalline Fe-18Cr-13Ni(100). *Corros. Sci.* **140**, 205–216 (2018).
10. Lince, J. R., Didziulis, S. V., Shuh, D. K., Durbin, T. D. & Yarmoff, J. A. Interaction of $O_2$ with the $Fe_{0.84}Cr_{0.16}(001)$ surface studied by photoelectron spectroscopy. *Surf. Sci.* **277**, 43–63 (1992).
11. Maurice, V., Yang, W. P. & Marcus, P. XPS and STM study of passive films formed on Fe-22Cr(110) single-crystal surfaces. *J. Electrochem. Soc.* **143**, 1182–1200 (1996).
12. Maurice, V., Yang, W. & Marcus, P. X-ray photoelectron spectroscopy and scanning tunneling microscopy study of passive films formed on (100)Fe-18Cr-13Ni single-crystal surfaces. *J. Electrochem. Soc.* **145**, 909–920 (1998).
13. Lampimäki, M., Lahtonen, K., Jussila, P., Hirsimäki, M. & Valden, M. Morphology and composition of nanoscale surface oxides on Fe-20Cr-18Ni(111) austenitic stainless steel. *J. Electron Spectrosc. Relat. Phenom.* **154**, 69–78 (2007).
14. Jussila, P., Lahtonen, K., Lampimäki, M., Hirsimäki, M. & Valden, M. Influence of minor alloying elements on the initial stages of oxidation of austenitic stainless steel materials. *Surf. Interface Anal.* **40**, 1149–1156 (2008).
15. Fujiyoshi, H., Matsui, T. & Yuhara, J. Segregation and morphology on the surface of ferritic stainless steel (001). *Appl. Surf. Sci.* **258**, 7664–7667 (2012).
16. Ibach, H. *Physics of Surfaces and Interfaces* (Springer, Berlin, Heidelberg, 2006).
17. Wiame, F. Strategies for the growth of large-scale self-organized structures. *Thin Solid Films* **642**, 258–275 (2017).
18. Kopatzki, E. & Behm, R. STM imaging and local order of oxygen adlayers on Ni (100). *Surf. Sci.* **245**, 255–262 (1991).
19. Stanka, B., Hebenstreit, W., Diebold, U. & Chambers, S. Surface reconstruction of $Fe_3O_4$(001). *Surf. Sci.* **448**, 49–63 (2000).
20. Stoltz, D., Onsten, A., Karlsson, U. & Göthelid, M. Scanning tunneling microscopy of Fe- and O-sublattices on $Fe_3O_4$(100). *Ultramicroscopy* **108**, 540–544 (2008).
21. Fonin, M. et al. Surface electronic structure of the $Fe_3O_4$(100): evidence of a half-metal to metal transition. *Phys. Rev. B* **72**, 104436 (2005).
22. Weiss, W. & Ranke, W. Surface chemistry and catalysis on well-defined epitaxial iron-oxide layers. *Prog. Surf. Sci.* **70**, 1–151 (2002).
23. Woodruff, D. P. Quantitative structural studies of corundum and rocksalt oxide surfaces. *Chem. Rev.* **113**, 3863–3886 (2013).
24. Liu, Y. et al. Enhanced oxidation resistance of active nanostructures via dynamic size effect. *Nat. Commun.* **8**, 14459 (2017).
25. Weiss, W. & Ritter, M. Metal oxide heteroepitaxy: Stranski-Krastanov growth for iron oxides on Pt(111). *Phys. Rev. B* **59**, 5201–5213 (1999).
26. Condon, N. G. et al. Biphase ordering of iron oxide surfaces. *Phys. Rev. Lett.* **75**, 1961–1964 (1995).
27. Chambers, S. & Joyce, S. Surface termination, composition and reconstruction of $Fe_3O_4$(001) and γ-$Fe_2O_3$(001). *Surf. Sci.* **420**, 111–122 (1999).
28. Soldemo, M., Lundgren, E. & Weissenrieder, J. Oxidation of Fe(110) in oxygen gas at 400 °C. *Surf. Sci.* **644**, 172–179 (2016).
29. Condon, N. G. et al. Biphase ordering on $Fe_3O_4$(111). *Phys. Rev. B* **55**, 15885–15894 (1997).
30. Shaikhutdinov, S. K., Ritter, M., Wang, X.-G., Over, H. & Weiss, W. Defect structures on epitaxial $Fe_3O_4$(111) films. *Phys. Rev. B* **60**, 11062–11069 (1999).
31. Bowker, M. et al. Surface structure of γ-$Fe_2O_3$(111). *Surf. Sci.* **606**, 1594–1599 (2012).
32. Tang, Y., Qin, H., Wu, K., Guo, Q. & Guo, J. The reduction and oxidation of $Fe_2O_3$(0001) surface investigated by scanning tunneling microscopy. *Surf. Sci.* **609**, 67–72 (2013).